Properties of AgBiI4 using high through-put DFT and machine learning methods

Victor T. Barone¹, Blair R. Tuttle²* and Sanjay V. Khare¹

Department of Physics, University of Toledo, Toledo, OH 43606 USA

Department of Physics, Penn State Behrend, Erie, PA 16563 USA

*Corresponding Author: brt10@psu.edu

Abstract

Silver iodo-bismuthates show promise for optoelectronic and other applications. Within this family of materials, AgBiI₄ is a prominent model compound. The complexity of AgBiI₄ has prevented a conclusive determination of the specific atomic arrangements of the metal atoms in the bulk material. Here we employ high through-put density functional and novel machine learning methods to determine 53 physically relevant unit cell configurations. We also calculate the fundamental properties of the bulk material using the newly discovered configurations. Our results for the lattice constant (12.7 Å) and band gap (1.8 eV) agree with previous theory and experiment. Finally, we report new predictions for the temperature-dependent conductivity mass for electrons ($\sim m_0$ at T=300K) and holes ($\sim 8m_0$ at T=300K); these masses will be useful in studies of AgBiI₄-based device simulations.

I. Introduction

Metal halide semiconductors are a new promising class of materials under development for various applications including flexible electronics, optoelectronics and radiation detectors.[1-5] Specifically, silver iodo-bismuthates – i.e., compounds with a generic formula Ag_xBi_yI_{x+3y} – have captured significant research interest as safer alternatives to mainstream lead-halide perovskite semiconductors. Importantly, these compounds can be grown through simple, low-cost, solution-based methods in thin films over flexible substrates.[4, 6-8] Because they are good photon absorbers, these materials hold promise for a variety of optoelectronic devices, including photovoltaics and photodetectors [6-9].

The structure [6, 10] and phase diagram [11] of Ag-Bi-I crystals have only recently been examined in detail. Given that the unit cells are large and complex, many calculations are needed to fully enumerate the possible unit cells of these crystals [8]. Here we focus on AgBiI₄, a prominent embodiment of the silver iodo-bismuthate family, which has been found to display a cubic crystal structure in many of its occurrences.[6, 10, 12] For AgBiI₄ the singly valent metal cation is Ag, the triply valent cation is Bi, and the singly valent anion is I. Other compounds, such as AgBi₂I₇, appear to be silver deficient versions of cubic AgBiI₄.[10]

Despite the importance of AgBiI₄, the atomic positions for the Ag and Bi atoms in the crystal have not been clearly established, mainly because of the complexity of the unit cell. The AgBiI₄ crystal includes cubic unit cells with two fixed sublattices; one sublattice includes iodine (I) atoms and the other includes Ag and Bi atoms. Because of the disorder in the position of Ag and Bi atoms there are thousands of possible unit cell configurations that can make up the bulk crystal. For AgBiI₄, previous calculations have employed a few sample structures and found structural properties and electronic band gaps in agreement with experiments.[10, 12] Despite these early successes, to confidently predict AgBiI₄ properties, e.g. for defects observed therein,[13] requires a clear understanding of the atomic structures present in device quality materials.

To identify the atomic positions in AgBiI4 crystals and to clarify the crystal properties, we sorted all possible unit cell configurations from low to high energy. During growth conditions, we find approximately 60 unit cells will be most present in bulk AgBiI4. Using hybrid density functional methods including spin orbit coupling, we calculate the band gap to be 1.8 eV, in agreement with experiment. Considering only the lowest energy unit cells would lead to an overestimation of the band gap. We report the Boltzmann averaged electronic density of states for AgBiI4 and determine the temperature-dependent conductivity masses. For both electrons and holes, mass increases with temperature.

II. Models and Methods

a) unit cell models

Experimentally, AgBiI₄ has been reported to have a cubic unit cell with a space group of Fd3m.[6, 10] The unit cells include a cubic-closed packed sub-lattice of 32 iodine atoms and a cation sublattice with all tetrahedral sites vacant. The cation sub-lattice has 16 sites and each site can have either a bismuth (Bi) or a silver (Ag) atom. To determine the number of combinations that are possible, we use the binomial equation. In general, for n sites with k sites occupied by Bi atoms and m = n - k sites occupied by Ag atoms, the number of combinations (C_k^n) can be written as $C_k^n = \frac{n!}{k!(n-k)!}$. In this case, with n = 16 and k = 8, there are 12,870 possible unit cell configurations, although many are equivalent by symmetry operations. For finding symmetry groups we used SpGLib [14] which found 72 % of the cells had no symmetry (P1). If the distribution of actual cells present in device quality films is controlled by thermodynamics, then the low energy cells will be most prevalent. Figure 1(a) shows a ball-and-stick representation of the lowest energy unit cell for AgBiI₄, based on the results of our calculations discussed below. Figure 1(b) shows atomic positions of the same model cut in slices along the c axis, which is the vertical axis in 1(a). In both images, the small black balls are iodine, the blue balls are bismuth, and the grey balls are silver atoms.

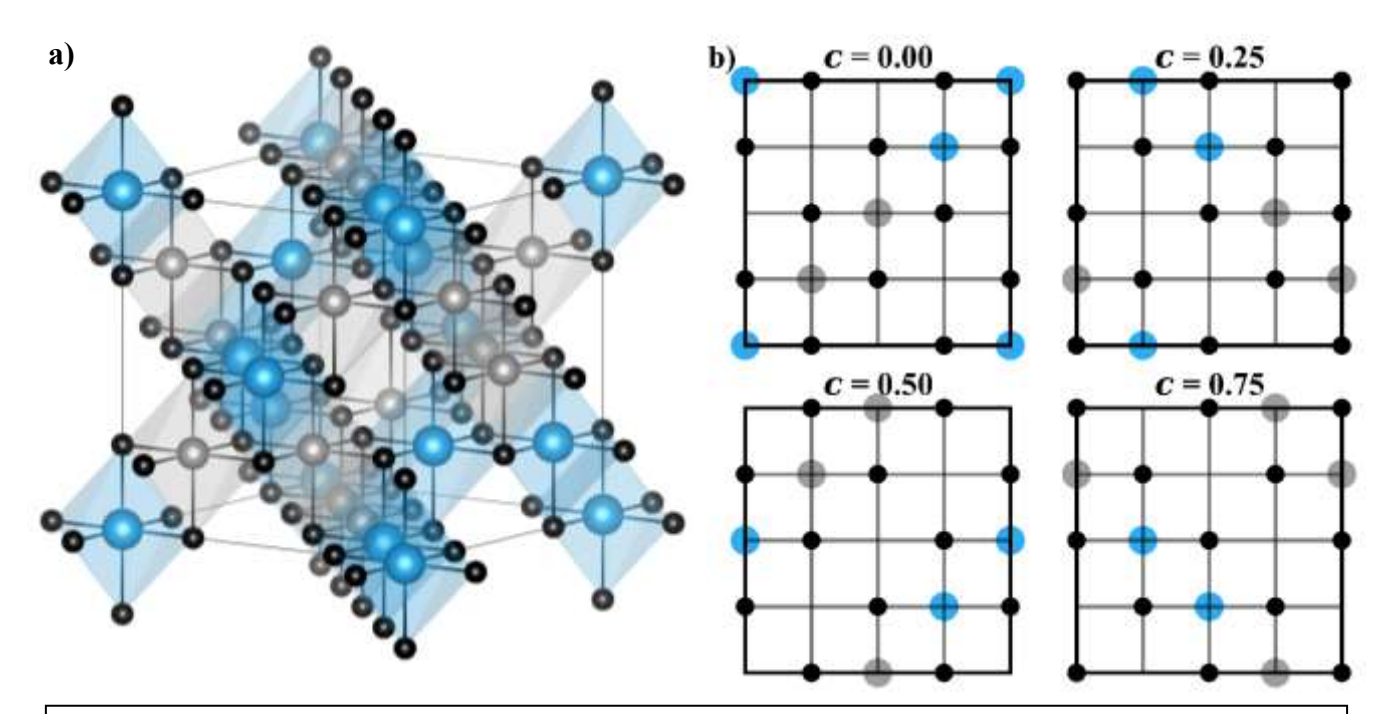


Figure 1: (a) A ball-and-stick representation of the lowest energy unit cell discovered in this investigation. The shaded regions show the silver and bismuth centered octahedra. (b) The same unit cell represented as layers on the c axis to show the topology more clearly. In both images, the small black balls are iodine, the blue balls are bismuth, and the grev balls are silver atoms. Note that $c = 0.00 \equiv c = 1.00$.

b) high through-put method

To determine the low energy unit cell structures, we employ a multi-level high through-put code employing efficient electronic structure calculations. Specifically, we use the Vienna Ab Initio Simulation Package (VASP [43], [44] version 5.4.1) for density functional calculations.[15, 16] We

treat exchange-correlation effects with the semi-local Perdew-Burke-Ernzerhof (PBE) functional.[17] Standard PAW potentials are used to represent the core-electrons. [45], [46] For the plane-wave basis function expansion, the cutoff energy used is 250 eV.

For the first level of calculations, only the Gamma point is used for Brillouin zone integrations. Also, the unit cell lattice constants are fixed at the experimental value. Atomic positions are relaxed until forces reach a tolerance of 0.05 eV/Å. We have written our own set of programs for managing large numbers of VASP simulations called VBHTC [18]. The code creates the VASP input files, automatically submits jobs to a computer with resources shared among multiple users, checks for job completion and resubmits jobs automatically.

From these initial calculations, low energy structures were identified for further consideration. For the next level calculations, we keep the same parameters as above except for the following changes. A single special k-point at ½ (111) is used. The force tolerance is lowered to 0.02 eV/Å. In addition to atomic position relaxations, we also determine the lattice constants by fitting energy-volume curves to each cell.

Finally, we selected cells whose probability of appearing in bulk material was highest. All lowest-energy cells whose combined probability of appearing in bulk AgBiI4 summed to 95% (according to a Boltzmann distribution with $k_BT=0.05~{\rm eV}$) were kept for further analysis. For these cells, more accurate relaxations were performed including a $3\times3\times3$ k-point grid and a force tolerance of $0.01~{\rm eV/Å}$ for atomic relaxations. With these calculation parameters, we also compute the Bulk modulus of each cell. For density of states calculations, we used finer grids of K-points and the Blöchl corrected tetrahedron method [50] was used to set partial occupancies.

c) analysis methods

Physical properties such as lattice parameters, simulated XRD patterns, density of states, and bulk moduli are averaged according to a Boltzmann distribution including unit cells with the lowest energy in the following way: if A(n) represents some physical property A of the nth unit cell, then we report the expected value of A, $\langle A \rangle$, for bulk AgBiI₄ as

$$\langle A \rangle = \sum_{n} P(n)A(n)$$

$$P(n) = \frac{1}{Z} \exp\left(-\frac{\varepsilon_n}{k_B T}\right)$$

where P(n) represents the probability of a state n, Z is the partition function, ε_n is the energy of the n^{th} state relative to the global minimum energy, and $k_{\text{B}}T=0.05$ eV to represent a synthetization temperature of around 600 K.

The density of electronic states for select models were evaluated on a $4 \times 4 \times 4$ k-point mesh at the PBE level. A correction to the PBE band gap was determined with a second set of calculations using a $2 \times 2 \times 2$ k-point mesh and the inclusion of hybrid exchange [19] + spin-orbit coupling. The effective masses are calculated at the PBE level as a thermal average over all bands and the entire Brillouin zone, as described by Hautier *et al* [20]. This method considers bands that are close to one another and non-parabolic bands. This is especially important for the valance bands in AgBiI₄. The Brillouin zone integration was performed on a $91 \times 91 \times 91$ grid with k values interpolated as weighted averages between the less densely packed PBE calculated k-points.

d) machine learning method

The computational cost of finding the energy of thousands of unit cells is prohibitive. Also, for other Ag-Bi-I systems, the number of unit cells to be considered is orders of magnitude larger. Therefore, we developed a machine learning method to reduce the computational load for finding low energy cells. The method employs a Random Forest (RF) model from Python's scikit-learn package.[21] The features of the RF model include Ag or Bi at each of the 16 cation sites along with the number of neighbors for each metal pair. Other features such as center of mass and space group identifiers were tested but provided little additional benefit. The low energy cells were discovered using the VBHTC [18] code for coupling the RF and VASP calculations in a high through-put fashion.

Three RF implementations were tested to search for the lowest energy unit cells. VASP Γ-point results were used for training all RF models. In version 1, the site occupancies were included in the RF feature set but without any description of the neighbor pair counts. In version 2, the neighbor pair counts were added to the feature set. In version 3, the feature set is the same as in version 2 but the RF model is forced to train on low energy unit cells. Specifically, version 3 uses the following routine: (1) Initialize the RF model with a random set of 100 unit cell results from the total. (2) Use the RF model to predict energies of the remaining unit cells. (3) Keep (around) 20% of the unit cells with predicted lowest energy structures. (4) Choose 100 models from the kept set to add to the RF model's training data. (5) With the trained RF model, re-estimate the energies of the all unit cells. (6) repeat steps (3)-(5) until 20 % of the kept set is less than 100.

III. Preliminary Results

Our initial energy calculations for all possible AgBiI₄ unit cells results in detailed information about the unit cell energetics and its relation to bonding topology. In addition, we present the energetics predicted by three random forest models and compare them to the DFT results.

a) energetics

The initial screening of all 12,870 AgBiI₄ unit cell structures allows us to organize each unit cell according to its energy. In Figure 2, an energy histogram is reported which shows that the unit cell energies span about 3 eV from the lowest to highest energy cells. The peak of the histogram occurs at around 1 eV above the minimum energy. Using the Boltzmann probability distribution from Section II.c., over 12,000 unit cells are more than 0.5 eV above the energy of the minimum energy cells and are not expected to be present in device quality samples of AgBiI₄. For the prediction of physical properties in Section IV, we only kept unit cells with an energy less than 0.2 eV above the minimum energy found. The 53 lowest-energy unit cells lie within the first bin and together represent 95% of the expected configurations in bulk AgBiI4.

The 53 unit cells can be split into two energy groups that are 0.11 eV apart from one another. Within those groups, the energy

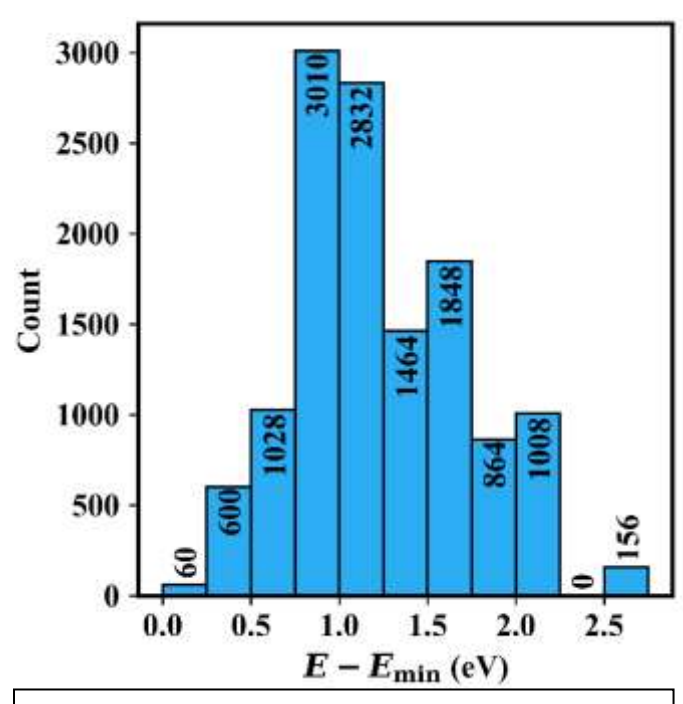


Figure 2: Energy histogram for all possible AgBiI₄ unit cells. The energy E is relative to the minimum cell energy, E_{\min} . The number of cells in each bin is shown at the top of the bin.

difference between cells are 1 meV or less. Further analysis of the lowest-energy group (including 12 unit cells) reveals that, from their initial coordinates, they are equivalent to one another through translational and rotational symmetry.[14] The higher energy group's structures are significantly more complex than the lower energy groups', as discussed below.

We performed an analysis of metal pairs in order to better understand the role of these atoms on the energetics of AgBiI₄. For Ag and Bi atoms, we define nearby metal neighbors to be within 4.5 Å of one another. Interestingly, the number of initial Ag-Ag pairs (before any relaxations) is a good indicator of the final relative energies, as seen in Figure 3. While all 12870 results are included in the figure, many data points overlap. The number of Ag-Bi and Bi-Bi pairs is also a good indicator, as they are directly related to the number of Ag-Ag pairs. The same relation gives an identical slope of 0.32 eV for Bi-Bi pairs. Also, there is a slope of -0.16 eV for Ag-Bi pairs.

The number of Ag-Ag and Bi-Bi interactions is strongly correlated to the energy of the unit cell structure. As discussed in **Sections II.d** and **III.b**, the pair count info is essential for creating an efficient RF model. Although ionic relaxation lowered system energies

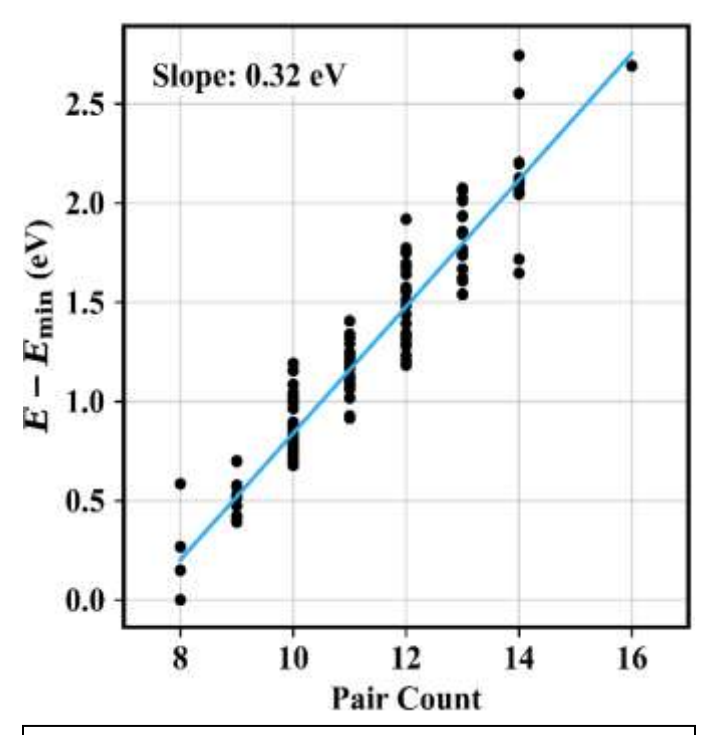


Figure 3: Relation between post-relaxation energy E (scaled by the minimum E_{\min}) and pre-relaxation Ag-Ag pair counts.

considerably, the lowest energy models were clearly those that started in a favorable state. In the lowest energy models, each cation has exactly two identical-element pairs, which minimizes the total pair count for the entire cell to 8. Variance in the energy-pair count relationship shown in **Figure 3** is due to ionic relaxations.

The ionic relaxations in a cell are correlated to the model's energetics with low energy models having low relaxation energies. Ag showed the most relaxation due in part to it being the lightest of the three elements. Over all 12,870 models, the average (maximum) relaxation from ideal positions for Ag, Bi, and I ions were 0.35 (0.98), 0.14 (0.29), and 0.14 (0.44) Å, respectively. Meanwhile, for the 53 unit cells with the lowest energy, these same relaxation values are 0.12 (0.21), 0.07 (0.09), and 0.10 (0.17) Å, respectively.

The topological properties of the neighbor chains are interesting. **Figure 4** shows the Ag-Ag (grey) and Bi-Bi (blue) pairs for the lowest energy unit cell. When atom pairs of the same element are arranged in the spiral-like pattern shown in **Figure 4a**, the number of Ag-Ag / Bi-Bi interactions is

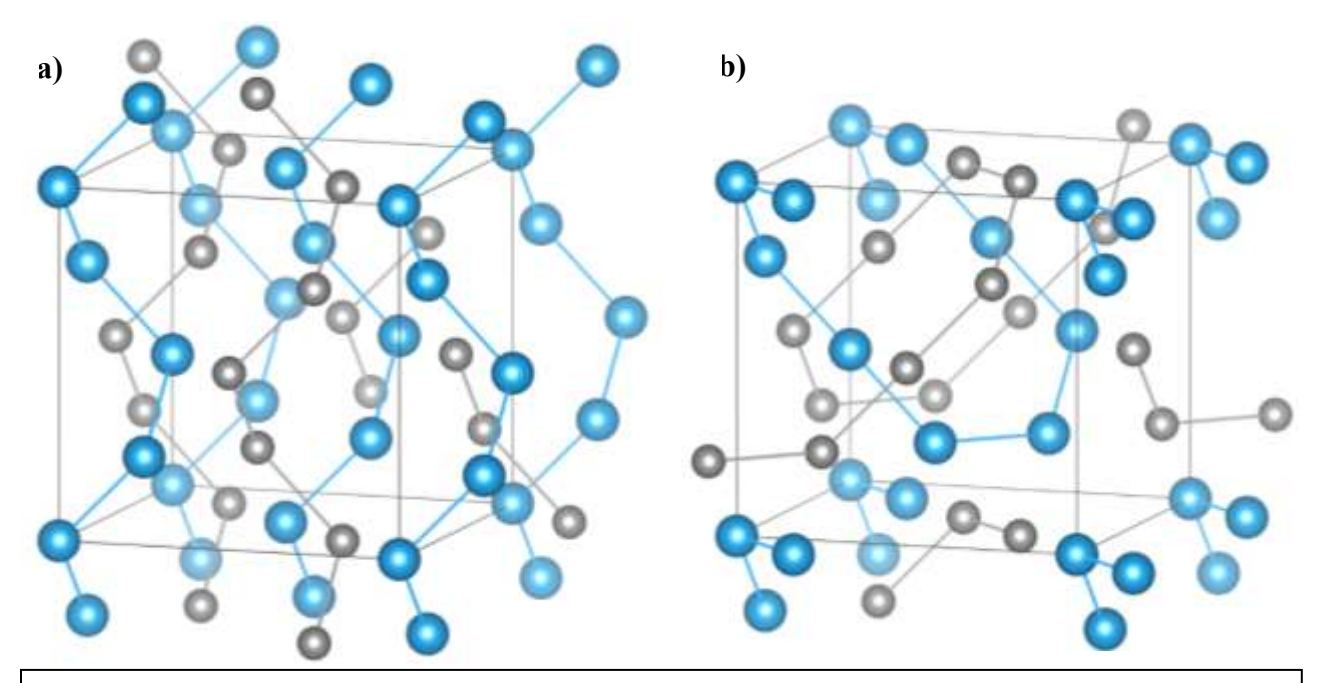


Figure 4: Identical-element metal neighbors present in low-energy AgBiI₄ unit cells. Ag-Ag pairs (grey) and Bi-Bi pairs (blue) are shown, while both Ag-Bi pairs and I atoms are omitted for clarity. (a) Spiral-like patterns present in the lowest-energy AgBiI₄ structures. Each Ag and Bi atom has two identical-element metal neighbors. (b) Second lowest-energy structures contain identical-element neighbors that loop around one another. Each atom also has two identical-element metal neighbors.

minimized (only two interactions per atom), and the cell energy is also minimized. All 12 of the lowest energy structures contain the spiral pattern of Ag-Ag and Bi-Bi pairs as illustrated in **Figure 4a**. Further, each unit cell is equivalent to the other through translational and rotational symmetry. Half have the space group P4₃22, and the other half the space group P4₁22. [14] Note that the difference between a 4₁ and 4₃ screw axis is simply the handedness of the operation. The remaining 41 models with slightly higher energies also contain structures that minimize the number of Ag-Ag / Bi-Bi interactions (2 per atom), but have more complicated chains of identical-element pairs. **Figure4b.**, for example, shows a higher energy structure that contains identical element pairs that 'loop' around one another. Each of these structures are reported to have the C222₁ space group. The reason for the difference in energy may be that there are fewer Ag-Bi pairs in these structures than there are in the spiral-like structures. For clarity the Ag-Bi pairs are not connected in **Figure 4**.

b) Random Forest Convergence

Figure 5 compares the predictions of three different versions of the RF model. In Figure 5 (a), the RF model features include no cation pair info and there is no search space reduction; (b) the RF model features include cation pair info, but there is no search space reduction; and (c) the RF model features include cation pair info and search space reduction is (as described in Section II.d) applied. In all cases, 500 points were used for training. The blue line represents an ideal 1:1 relationship between RF energetics and DFT energies. In order to keep the number of training points constant between methods, the search space is reduced by a factor of 0.672 for Figure 5(c).

All three RF model predictions show a positive correlation with the calculated DFT energies. Comparing **Figure 5(a)** and **Figure 5(b)** indicates that large improvement in RF model energies is achieved by including the cation pair data. However, in **Figure 5(b)** there is still significant error in the minimum energy models; specifically, there is an energy span of about 0.4 eV near the minimum where the RF model's standard error is around 0.12 eV. As seen in **Figure 5(c)**, the RF model which trains on lower energy cells results in a much more accurate prediction of the lowest energy cells although the average error in energies across the entire dataset is worse. Within the same 0.4 eV energy span near the minimum energy, the accuracy of the RF model in **Figure 5(c)** is about 0.02 eV – six times smaller than the error found in the **Figure 5(b)** results.

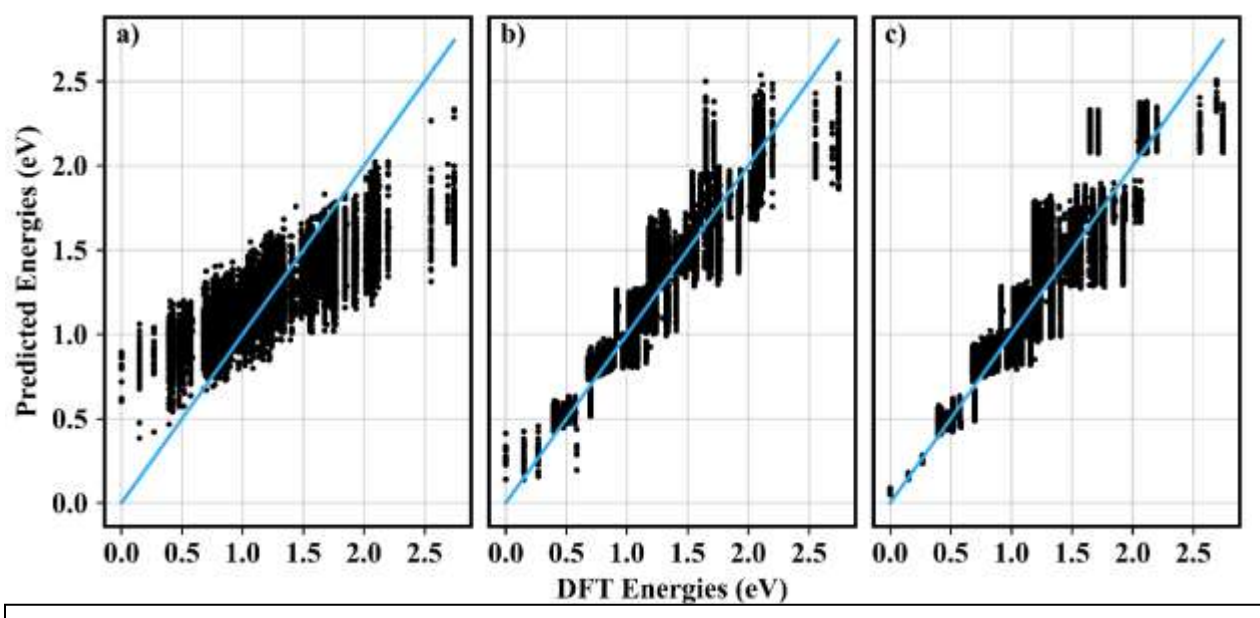


Figure 5: Predicted energies for three different machine learning methods as a function of the level 1 DFT energies from the high through-put method. The full AgBiI₄ dataset although many data points overlap in the figures above.

IV. Physical Properties

Here we report DFT calculations for the structural and electronic properties of AgBiI₄. Unless otherwise noted, all reported values are given as weighted averages, which is described in **Section II.c** above.

a) structural properties

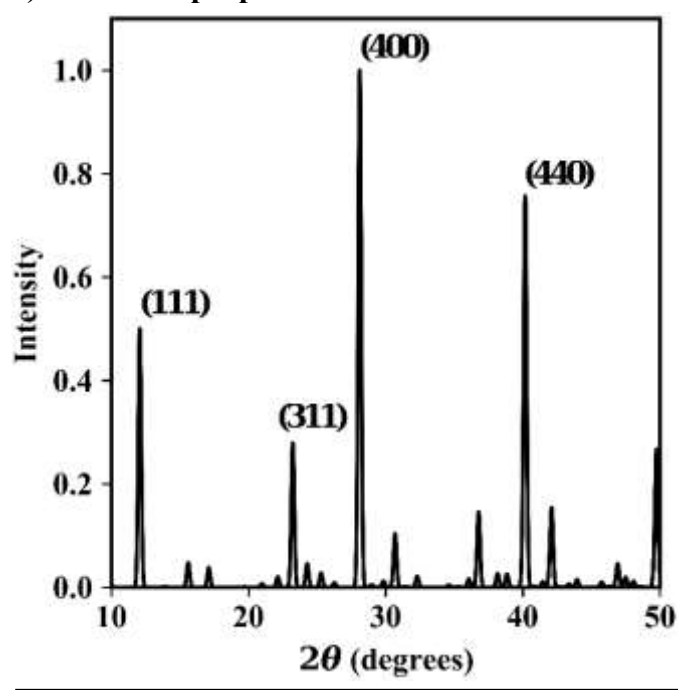


Figure 6: Computed X-ray diffraction pattern and Miller indices for AgBiI₄.

We computed the average lattice constant of AgBiI₄ to be 12.69 Å, about +4% greater than experiments[12, 22-24] but close to the previous theoretical calculations using one AgBiI₄ model [10, 13]. The +4% deviation experimental values is within expectations for DFT-GGA calculations. Further, both Bi-I and Ag-I bond lengths were found to be 3.14 Å, close to the experimental value of 3.09 Å [24]. The calculated density is $\rho = 5.3 \text{ g/cm}^3 \text{ differs from the experimental}$ value of 6 g/cm³ [24] due to the aforementioned overestimation of lattice constants. This result is close to Xiao et al's theoretical value of $\rho = 5.2 \text{ g/cm}^3$ [10].

The simulated x-ray diffraction (XRD) pattern is reported in **Figure 6** and compares well with experiment. In our calculations, $\lambda = 1.5406$ Å (Cu K- α radiation) was used to match experimental values. Also, we used a constant Debye-Waller factor of 0.2 Å².

Sansom *et al.*'s [12] experimental XRD pattern comes from polycrystalline AgBiI₄ films and has peak angle and intensities in very good agreement with our simulated XRD pattern. There is also good agreement with Ghosh *et. al.*'s [25] experimental XRD pattern except for their lower intensity at the (440) peak, possibly due to the texturing effect inherent in polycrystalline films

b) mechanical properties

The bulk modulus K has an average value of 7.6 GPa. This value is in between the theoretical K values for AgI (K = 20 GPa) and BiI₃ (K = 4 GPa) [26]. For the 12 lowest energy structures, $\langle K \rangle = 7.7$ GPa, with a range of 7.3 < K < 8.3 GPa. The 41 higher energy structures have $\langle K \rangle = 7.5$ GPa and exhibit a range of values: 7.1 < K < 8.0 GPa. In both groups, the values of K show a single peaked, normal distribution.

c) electronic structure

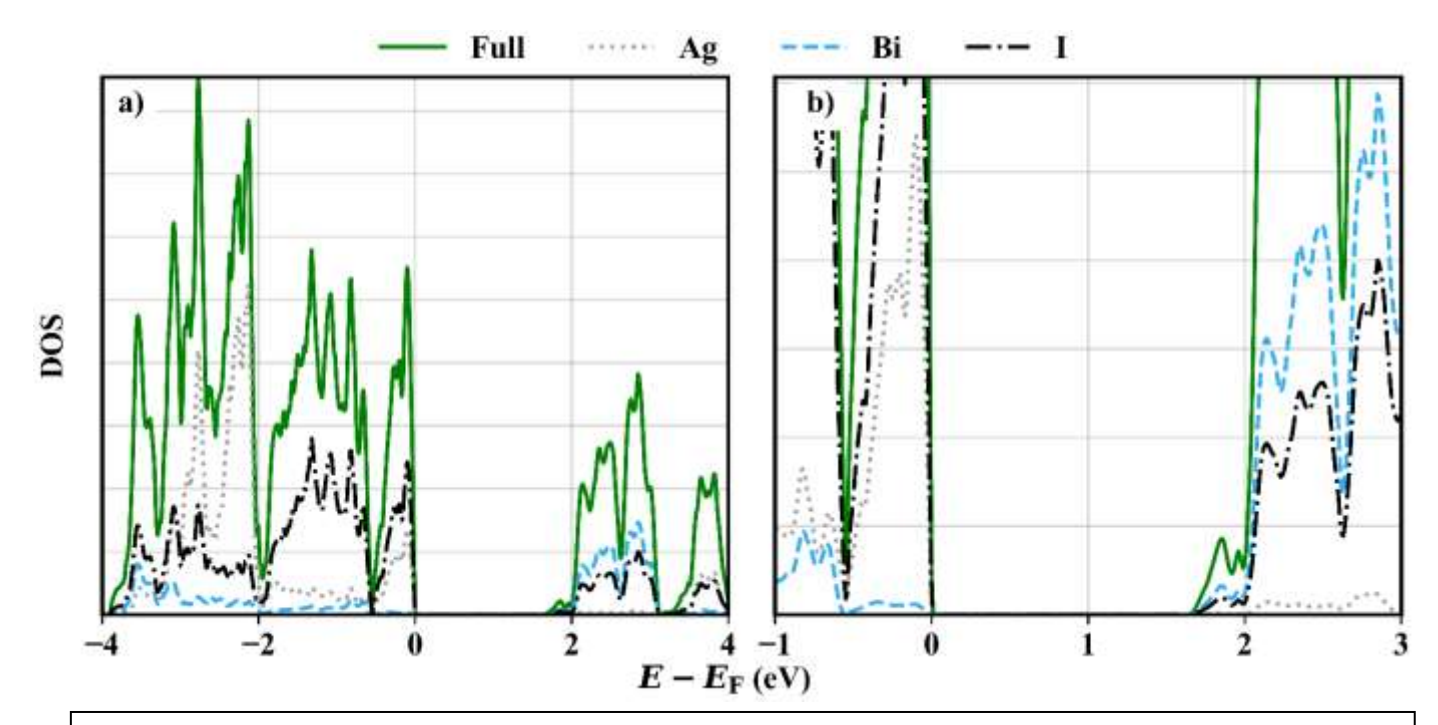


Figure 7: (a) Average atom-DOS for the 53 lowest energy AgBiI₄ cells. Each element is plotted as the sum of its l = 0,1,2 states, and the energy E is scaled by the Fermi energy E_F . (b) Zoom-in of (a) to show the element contributions to the band maxima more clearly.

Figure 7 shows the Boltzmann averaged DOS for the 53 low energy AgBiI₄ structures split by each element's contribution. Ag (l = 2) and I (l = 1) are the major contributors to the DOS near the

valence band maximum, while Bi and I states (both l = 1) dominate near the conduction band minimum. These results are consistent with the findings from previous theoretical studies.[12] The DOS of the 12 lowest energy cells (those with the spiral-like identical-element pair topologies) and the 41 higher energy cells (those with the loop-like identical-element pair topologies) are very similar except that the higher energy cells have conduction states below 2 eV. In the lowest energy cells, there are no states until after 2 eV. Since AgBiI₄ is known to have a band gap below 2 eV, this is evidence that the bulk material contains some appreciable amount of higher energy unit cell configurations.

The DOS in Figure 7 is calculated with the PBE functional, but previous calculations show that including hybrid exchange and spin-orbit effects raises the band gap slightly Upon the inclusion of both hybrid [10]. exchange and spin-orbit effects for five models, we find that the band gap increases on average by 0.12 eV. Therefore, our theoretical estimate for the band gap of AgBiI₄ is 1.8 eV. This is in good agreement with previous experimental results of 1.7 eV [12, 22, 25], 1.8 eV [6], and 1.9 eV [27]. The band gap value found here also agrees with previous theoretical calculations using similar methods on a single model,[10] suggesting the model previously used is not among the lowest energy models we found (since we found the lowest energy models have band gaps greater than 2 eV).

d) effective masses

To properly account for the degenerate bands and relatively flat valance bands near the band edge, we calculate a thermal average conductivity mass that includes contributions

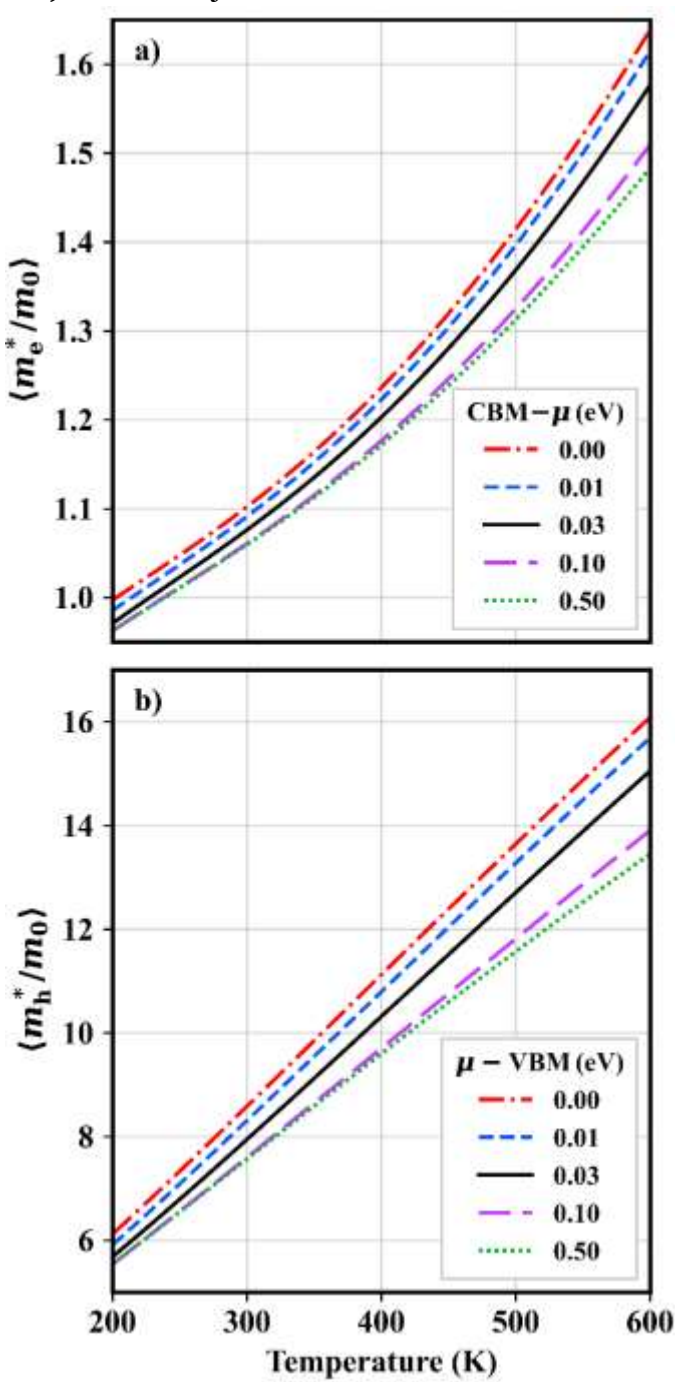


Figure 8: Conductivity (a) electron and (b) hole effective masses in AgBiI₄. Averages are taken over the three characteristic directions calculated from the full m^* tensor. Chemical potential values, μ , are given relative to their relevant band maxima.

from multiple bands and their non-parabolicities. Because the higher energy group of cells have conduction band states about 0.3 eV below the lowest energy cells', electron transport is expected to be dominated exclusively by the second lowest energy group of cells. Thus, electron effective masses are only calculated with a model from the higher energy group. On the other hand, we calculate the hole masses with a weighted average of one low energy cell's (85% contribution) and one high energy cell's (15% contribution) conductivity masses. This weighted average is an approximation to the full Boltzmann averaging done in the rest of this work, but is necessary because of the computational cost needed for thermal average effective mass calculations.

Figure 8 shows the average conductivity mass (calculated from the Drude model as the harmonic mean of the three eigen-masses (m^*) in AgBiI₄) plotted vs. temperature for various chemical potentials. The relative masses increase monotonically with temperature from 200 to 600 K. Near room temperature, we find m^* for n-doped AgBiI₄ to be about that of a resting electron. Due to the relatively flat valance bands in AgBiI₄, hole effective masses are very heavy— about eight times heavier than a resting electron at room temperature. Between 200K and 600K, electron masses increase by about a factor of 1.6, and hole masses by about 2.7.

In general, m^* increases with temperature, since raising the temperature thermally activates (1) non-parabolic portions of bands and (2) states further from the band edges, which tend to be flatter than states at the band edges. These two effects also explain why m^* increases as the Fermi energy moves closer to the band edges.

e) band structure

A better understanding of the thermal average conductivity mass can be obtained through an inspection of the band energies. **Figure 9.a** shows the energy-map of the lowest energy model's valance band while **Figure 9.b** show the energy-map for conduction band edges of a model from the second lowest energy group. Note that $1/8^{th}$ of the Brillouin zone is removed to more clearly portray the energies around the Γ point as well as the different scaling between **a** and **b**.

In **Figure 9.a**, the red-orange domains of high energy and low curvature extend from Γ most dramatically to the edges in the $\pm k_x$ direction. These shallow regions increase the effective hole masses even below room temperature. **Figure 9.c** shows secondary bands that will affect hole masses at elevated temperatures. From **Figure 9.d**, at the R point two bands are nearly degenerate, with the higher energy band having a higher energy curvature. The energy difference between these two bands is small enough that the thermal average takes the higher curvature band into account except at temperatures far below room temperature.

Even temperatures below temperature, the conductivity masses can significantly differ from effective masses calculated with the standard parabolic approximation. For example, consider the valance bands in a low energy model of AgBiI₄ (Figure 9.a, 9.c). In the [100] direction (corresponding to the direction of the spiral patterns in Figure 4.a), bands at the band edge are very shallow – the difference between the top and bottom of the band maxima band is only about 15 meV. This means that, even at 87K ($k_BT = 7.5 \text{ meV}$), about half of the entire band is thermally activated. Additionally, the second topmost band is about 10 meV below the VBM, meaning that it will begin contributing to the average mass at around 120K. As for the conduction bands, the near-degenerate (10 meV difference in energies at the R point) bands at the conduction band edge (Figure **9.d**) exhibit similar curvatures in two of three directions, but the curvature of the higher in the [001] direction energy band significantly lowers the thermal average mass compared to only considering the lowest energy band in the parabolic

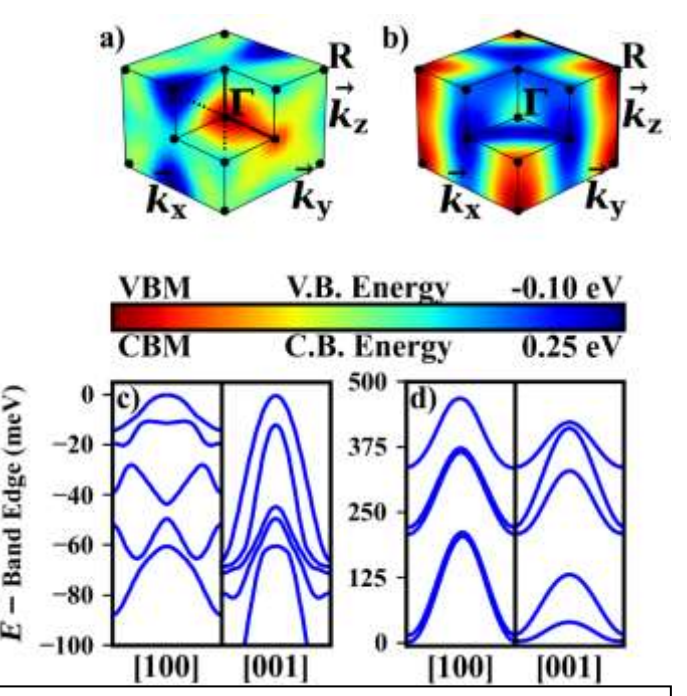


Figure 9: Energies of the valance band edge (a) and conduction band edge (b) in the 1st Brillouin zone of AgBiI₄. In (a), black lines originating from the VBM (Γ) represent paths that the valance band diagrams (c) are calculated along. Similarly, in (b), black lines originating from the CBM (R) represent paths that the conduction band diagrams (d) are calculated along.

approximation. This effect should also be seen at about 120K.

Pecunia et al [13] recently used the parabolic approximation to calculate effective masses in AgBiI₄. For electrons, they report conductivity masses of $1.1m_0$ which coincides with the present conductivity result at 200K. This is due to the harmonic averaging method – the lightest, middle, and heaviest electron masses from Pecunia et al are $0.9m_0$, $1.1m_0$, and $1.3m_0$, while our thermal average results at 200K are $0.7m_0$, $0.7m_0$, and $3.8m_0$. Although the individual masses differ, the average yields similar results. The same is not true for holes, where the previously reported conductivity mass is $4.3m_0$ is lower than our hole mass of $6m_0$ at 200K. Deviations between previous results and present results are likely due to both choice of unit cell(s) as well as previously discussed differences between thermal averaging and parabolic approximations to calculate the effective mass. As one would expect from the complicated valance bands of AgBiI₄, the differences between the parabolic results and thermal average results are larger for holes than for electrons and become increasingly larger at elevated temperatures.

V. Conclusion

By calculating the energies of all possible AgBiI₄ unit cells, we have determined a subset of cells which, when considered as an ensemble, produce results consistent with experiment. With these cells, we predict the material's mechanical and electrical properties, including the conductivity effective masses. For the latter, we quantify the variation in average band masses as a function of temperature and Fermi energy.

Additionally, we showcase a simple random forest model that is capable of accurately determining the lowest energy cells with a computational load reduced by a factor of 25. For predicting the final relaxed DFT energies of AgBiI₄, bonding topology was found to be an important factor. Combining a simple set of machine learning descriptors with an aggressive reduction of the unit cell search space allowed for the accurate classification of the lowest-energy unit cells. We believe that this method should be useful for solving similar problems involving large numbers of unit cells.

For properties such as the lattice constant and powder XRD pattern, many unit cells reproduce experimental results well. It is necessary, however, to include higher energy cells to reproduce the band gap, indicating that bulk AgBiI₄ contains significant contributions from slightly higher energy ($\Delta E \sim 0.1 \ eV$) unit cell configurations.

We predict that AgBiI₄ has a bulk modulus more similar to BiI3 than to bulk AgI. The DOS shows that Ag and I states make up the majority of the upper valance band, while the lower conduction band is comprised of Bi and I states, consistent with Ref. [12]. For AgBiI₄'s use in devices, average conductivity mass calculations indicate that relying on holes for charge transport will be very inefficient on account of their heavy masses, while electrons should provide more reasonable transport properties. These results are consistent with the band structure of AgBiI₄, which exhibits a high density of flat valance bands near the VBM, and a few conduction bands with higher curvatures near the CBM.

Of course, the properties of the whole material is not guaranteed to be the average of individual unit cell results. Nevertheless, the unit cells identified herein present a proper starting point for the study of the role of larger scale structures and for examining the properties of defects in AgBiI₄. Further, our approach and findings provide a platform for future studies of the structural and electronic properties of other silver iodo-bismuthate compounds and related metal-halide semiconductors.

VI. Acknowledgements

BRT would like to acknowledge support from National Science Foundation under grant DMR-2127473. Computations for this research were performed on the Pennsylvania State University's Institute for Computational and Data Sciences' Roar supercomputer.

REFERENCES

- [1] A. K. Jena, A. Kulkarni, and T. Miyasaka, "Halide Perovskite Photovoltaics: Background, Status, and Future Prospects," *Chemical Reviews*, vol. 119, no. 5, pp. 3036-3103, 2019/03/13 2019.
- [2] D. H. Fabini *et al.*, "Main-Group Halide Semiconductors Derived from Perovskite: Distinguishing Chemical, Structural, and Electronic Aspects," *Inorganic Chemistry*, vol. 56, no. 1, pp. 11-25, 2017/01/03 2017.
- [3] J.-C. Hebig, I. Kühn, J. Flohre, and T. Kirchartz, "Optoelectronic Properties of (CH3NH3)3Sb2I9 Thin Films for Photovoltaic Applications," *ACS Energy Letters*, vol. 1, no. 1, pp. 309-314, 2016/07/08 2016.
- [4] S. Sun, S. Tominaka, J.-H. Lee, F. Xie, P. D. Bristowe, and A. K. Cheetham, "Synthesis, crystal structure, and properties of a perovskite-related bismuth phase, (NH4)3Bi2I9," *APL Materials*, vol. 4, no. 3, p. 031101, 2016.
- [5] G. Kakavelakis, M. Gedda, A. Panagiotopoulos, E. Kymakis, T. D. Anthopoulos, and K. Petridis, "Metal Halide Perovskites for High-Energy Radiation Detection," *Advanced Science*, vol. 7, no. 22, p. 2002098, 2020.
- [6] I. Turkevych *et al.*, "Photovoltaic Rudorffites: Lead-Free Silver Bismuth Halides Alternative to Hybrid Lead Halide Perovskites," *ChemSusChem*, vol. 10, no. 19, pp. 3754-3759, 2017.
- [7] H. Zhu, M. Pan, M. B. Johansson, and E. M. J. Johansson, "High Photon-to-Current Conversion in Solar Cells Based on Light-Absorbing Silver Bismuth Iodide," *ChemSusChem,* vol. 10, no. 12, pp. 2592-2596, 2017.
- [8] A. Crovetto, A. Hajijafarassar, O. Hansen, B. Seger, I. Chorkendorff, and P. C. K. Vesborg, "Parallel Evaluation of the Bil3, BiOI, and Ag3Bil6 Layered Photoabsorbers," *Chemistry of Materials*, vol. 32, no. 8, pp. 3385-3395, 2020/04/28 2020.
- [9] V. Pecunia, "Efficiency and spectral performance of narrowband organic and perovskite photodetectors: a cross-sectional review," vol. 2, p. 042001, 08/30 2019.
- [10] Z. Xiao, W. Meng, D. B. Mitzi, and Y. Yan, "Crystal Structure of AgBi2I7 Thin Films," *The Journal of Physical Chemistry Letters*, vol. 7, no. 19, pp. 3903-3907, 2016/10/06 2016.
- [11] L. F. Mashadieva, Z. S. Aliev, A. V. Shevelkov, and M. B. Babanly, "Experimental investigation of the Ag–Bi–I ternary system and thermodynamic properties of the ternary phases," *Journal of Alloys and Compounds*, vol. 551, pp. 512-520, 2013/02/25/ 2013.
- [12] H. C. Sansom *et al.*, "AgBil4 as a Lead-Free Solar Absorber with Potential Application in Photovoltaics," *Chemistry of Materials*, vol. 29, no. 4, pp. 1538-1549, 2017/02/28 2017.
- [13] V. Pecunia *et al.*, "Assessing the Impact of Defects on Lead-Free Perovskite-Inspired Photovoltaics via Photoinduced Current Transient Spectroscopy," *Advanced Energy Materials*, vol. 11, no. 22, p. 2003968, 2021.
- [14] A. Togo and I. Tanaka, "\$\textttSpglib\$: a software library for crystal symmetry search," arXiv [cond-mat.mtrl-sci], 2018 2018.
- [15] P. Hohenberg and W. Kohn, "Inhomogeneous Electron Gas," *Physical Review,* vol. 136, no. 3B, pp. B864-B871, 11/09/1964.

- [16] W. Kohn and L. J. Sham, "Self-Consistent Equations Including Exchange and Correlation Effects," *Physical Review*, vol. 140, no. 4A, pp. A1133-A1138, 11/15/1965.
- [17] J. P. Perdew, K. Burke, and M. Ernzerhof, "Generalized Gradient Approximation Made Simple," *Physical Review Letters*, vol. 77, no. 18, pp. 3865-3868, 10/28/1996.
- [18] V. T. Barone, "VBHTC," ed, 2021.
- [19] J. Heyd, G. E. Scuseria, and M. Ernzerhof, "Hybrid functionals based on a screened Coulomb potential," *The Journal of Chemical Physics*, vol. 118, no. 18, pp. 8207-8215, 2003.
- [20] G. Hautier, A. Miglio, D. Waroquiers, G.-M. Rignanese, and X. Gonze, "How Does Chemistry Influence Electron Effective Mass in Oxides? A High-Throughput Computational Analysis," *Chemistry of Materials*, vol. 26, no. 19, pp. 5447-5458, 2014/10/14 2014.
- [21] F. Pedregosa *et al.*, "Scikit-learn: Machine Learning in Python," *J. Mach. Learn. Res.*, vol. 12, no. null, pp. 2825–2830, 2011.
- [22] M. Khazaee *et al.*, "Dual-source evaporation of silver bismuth iodide films for planar junction solar cells," (in en), *Journal of Materials Chemistry A*, vol. 7, no. 5, pp. 2095-2105, 2019 2019.
- [23] C. Lu *et al.*, "Inorganic and Lead-Free AgBil ₄ Rudorffite for Stable Solar Cell Applications," (in en), *ACS Applied Energy Materials*, vol. 1, no. 9, pp. 4485-4492, 2018/09/24/2018.
- T. Oldag, T. Aussieker, H.-L. Keller, C. Preitschaft, and A. Pfitzner, "Solvothermale Synthese und Bestimmung der Kristallstrukturen von AgBil4 und Ag3Bil6," (in de), Zeitschrift for anorganische und allgemeine Chemie, vol. 631, no. 4, pp. 677-682, 2005/03// 2005.
- [25] B. Ghosh *et al.*, "Superior Performance of Silver Bismuth Iodide Photovoltaics Fabricated via Dynamic Hot-Casting Method under Ambient Conditions," (in en), *Advanced Energy Materials*, vol. 8, no. 33, p. 1802051, 2018/11// 2018.
- [26] M. de Jong *et al.*, "Charting the complete elastic properties of inorganic crystalline compounds," *Scientific Data*, vol. 2, no. 1, p. 150009, 2015/03/17 2015.
- [27] S. Lu, Q. Zhou, Y. Ouyang, Y. Guo, Q. Li, and J. Wang, "Accelerated discovery of stable lead-free hybrid organic-inorganic perovskites via machine learning," *Nature Communications*, vol. 9, no. 1, p. 3405, 2018/08/24 2018.